Kinetics of stored and dissipated energies associated with cyclic loadings of dry polyamide 6.6 specimens

Adil Benaarbia, André Chrysochoos, Gilles Robert

Kinetics of stored and dissipated energies associated with cyclic loadings of dry polyamide 6.6 specimens

Adil Benaarbia [a,b,*], André Chrysochoos [a], Gilles Robert [b]

[a] University Montpellier 2, LMGC Laboratory, CNRS, Place Eugène Bataillon, 34095 Montpellier, France
[b] Solvay Engineering Plastics, Technyl Innovation Center-Simulation et Validation des, Applications, Avenue Ramboz, BP64, 69192 Saint Fons, France

Keywords:
Semi-crystalline thermoplastic matrix
Stored energy rate
Dissipation energy rate
Taylor & Quinney ratio
Infrared thermography
Digital image correlation

A B S T R A C T

An experimental protocol was developed to achieve complete energy balances associated with the low cycle fatigue (LCF) of dry polyamide 6.6 (PA6.6) matrix. The protocol uses two quantitative imaging techniques, infrared thermography (IRT) and digital image correlation (DIC). The first technique provides a direct estimate of heat sources, especially intrinsic dissipation and thermoelastic sources, using the local heat diffusion equation. The second technique gives access to the deformation energy by means of strain and stress assessments. Stresses were derived from strain measurements using a simplified local form of equilibrium equations. Both techniques were then successfully combined with the aim of quantifying various energies involved in the energy balance (e.g. deformation, dissipated and stored energies) and then to obtain an estimate of the Taylor-Quinney ratio. From a thermomechanical modeling standpoint, the experimental results exhibit some interesting findings during the first few cycles. It was found that there was neither mechanical nor thermodynamic cyclic stability. From a mechanical standpoint, a significant ratcheting phenomenon characterized by accumulation of cyclic strain is classically observed. From a thermodynamic viewpoint, it was shown that the dissipated energy per cycle was always less than the mechanical energy that could be associated with the area of the hysteresis loop. This energy difference reflects the significant contribution of the stored energy associated, cycle by cycle, with the microstructural changes. Moreover, a 2d full-field measurement analysis highlighted hot spots occurring in the dissipation fields. The surface detection of these spots was thus correlated with those of the thermoelastic source with the aim of monitoring the fatigue damage accumulation in the region where the crack finally occurred.

1. Introduction

Semi-crystalline polymers represent an important class of materials which are now widespread in various industrial areas, such as the automotive industry. These engineering materials are of particular interest because of their remarkable advantages, notably regarding their low density, high deformability, toughness and long lifespan. Although academic and industrial research has enhanced knowledge on fatigue mechanisms in these thermo-hygro-sensitive materials, further insight is required on some issues concerning the understanding of *i)* dissipative and stored energy changes, *ii)* the influence of the loading

* Corresponding author. University Montpellier 2, LMGC Laboratory, CNRS, Place Eugène Bataillon, 34095 Montpellier, France.
E-mail address: abenaarb@univ-montp2.fr (A. Benaarbia).

frequency and *iii)* the localization of fatigue damage. One promising approach for addressing these issues is based on energy considerations. A combined description of mechanical and energy phenomena occurring during the deformation process may shed greater light on the behaviour of these polymeric materials (see e.g. *Rittel (2000)* [1], *Rittel and Rabin (2000)* [2]).

When a material is subjected to irreversible transformations, part of the mechanical energy expended in the deformation process is converted into heat, with the rest remaining stored in the material, thereby modifying its internal energy. Many interesting surveys on specific aspects of the stored energy can be found in the literature. The most significant developments that have taken place in the computation and interpretation of the stored energy were closely related to calorimetric procedures. Most research has been focused on temperature rise measurements to estimate variations in this energy using different experimental equipment, ranging from embedded thermocouples, microcalorimeters to infrared detectors. The earliest available references on the subject were focused on metal studies. *Farren and Taylor (1925)* [3] and *Taylor and Quinney (1934)* [4] were the first to build an apparatus to measure stored energy during the deformation of metallic materials[1] subjected to quasi-static monotonous tensile tests. *Williams (1967)* [5] and *Leach (1970)* [6] reviewed calorimetric methods in detail and assessed procedures and equipment for calorimetry applicable to the measurement of stored energy. Most investigations have focused on the Taylor-Quinney ratio, which expresses the fraction of the anelastic deformation energy rate irreversibly converted into heat, i.e. dissipated. In addition, these earliest works were limited by the fact that they were mostly carried out with standard and traditional measurement devices that could not reliably obtain high precision estimates of this ratio. However, with the introduction of high resolution infrared scanners in the early 1980s, extensive experimental studies rectified these deficiencies and assessed the Taylor-Quinney coefficient with greater accuracy (see e.g. *Chrysochoos (1985)* [7], *Chrysochoos* et al. *(1989)* [8], *Mason* et al. *(1994)* [9], *Rittel (1999)* [10], *Rosakis* et al. *(2000)* [11], *Oliferuk* et al., *2004* [12]).

In practice, thermal, displacement and stress fields are required for evaluating the various quantities involved in the energy balance. The most convenient imaging techniques for measuring these fields are infrared thermography and digital image correlation. The first technique provides thermal images, and the heat sources associated with the material deformation are directly assessed using the local heat diffusion equation. The second technique gives access to surface displacement fields from which strains and strain rates are derived. The deformation energy rate can thus be calculated through local measurement of stress and strain rate fields. Both non-contact quantitative imaging techniques can then be combined to establish energy rate balances.

In the present paper we document some findings pertaining to the thermomechanical behavior of PA6.6 dry matrix. Specifically, we used infrared and CCD cameras to simultaneously record, during cyclic loading, fields corresponding to temperature variations and displacement over the sample gauge part. We focused particularly on the energy balance form associated with the mechanical hysteresis loop. In particular, we obtained energy balances at two different loading frequencies, thus providing the deformation, dissipated and stored energy patterns. We finally derived time courses of the Taylor-Quinney ratio in order to quantify the relative importance of both dissipated and stored energy rates over each cycle. In addition, we used 2D analysis to highlight the existence of hot spots in dissipation fields. The location of these spots was correlated with those of the thermoelasticity and could be interesting for tracking the onset and propagation of local failure.

First, we present a very brief overview of the theoretical framework used to interpret the experiments.

2. Governing equations

2.1. Thermodynamic foundations of the heat equation

The framework of Thermodynamics of Irreversible Processes (*Halphen and Nguyen (1975)* [13]), is hereafter used to introduce the energy terms. Under the hypothesis of small deformations, the thermal, mechanical and microstructural states of the material are described by the following observable state variables: the absolute temperature $T = \alpha_0$, the total strain tensor $\boldsymbol{\varepsilon} = \boldsymbol{\alpha}_1$ and the set of internal variables $\{\alpha_k\}_{k=1,\ldots,m}$. The chosen thermodynamic potential is the specific Helmholtz free energy $\psi = \psi(T,\boldsymbol{\varepsilon},\alpha_k)$. Using the scalar product of the following "flux" vector $(\dot{\boldsymbol{\varepsilon}}, \dot{\alpha}_k, \mathbf{q})$ and its conjugate vector of thermodynamic forces $(\boldsymbol{\sigma} - \rho\boldsymbol{\psi}_{,\boldsymbol{\varepsilon}}, -\rho\psi_{,\alpha_k}, -T^{-1}\mathbf{grad}T)$, the classical Clausius-Duhem inequality leads to [13]:

$$\mathcal{D} = \underbrace{\left(\boldsymbol{\sigma} - \rho\boldsymbol{\psi}_{,\boldsymbol{\varepsilon}}\right) : \dot{\boldsymbol{\varepsilon}} - \rho\psi_{,\alpha_k}\dot{\alpha}_k}_{\mathcal{D}_1} \underbrace{-T^{-1}\mathbf{grad}T\cdot\mathbf{q}}_{\mathcal{D}_2} \geq 0 \qquad (1)$$

where $\boldsymbol{\sigma}$, $\mathbf{q}$ and ρ are, respectively, the total stress tensor, the heat flux vector and the material density, while $\dot{\mathbf{x}}$ stands for the time derivative of the state variable $\mathbf{x}$, and the operator : denotes the tensorial contraction over two indices.

Traditionally, we assume that the intrinsic $\mathcal{D}_1$ and thermal $\mathcal{D}_2$ dissipation are separately non negative, i.e. $\mathcal{D}_1 \geq 0$ and $\mathcal{D}_2 \geq 0$. Next, we define the specific heat as $C_{\boldsymbol{\varepsilon},\alpha} = -T\psi_{,TT}$ at constant $\boldsymbol{\varepsilon}$ and α_k. By combining both principles of thermodynamics, one can directly obtain the standard local heat diffusion equation as follows:

[1] In their investigations, *Farren and Taylor (1925)* [3] measured the heat effect by the rise in temperature of the specimen using a thermocouple. Their so-called "cold work" was obtained from the area under the stress-strain curve. The authors estimated stored energy values of approximately 13.5% for steel, 6.5% for copper and 7% for aluminum.

$$\rho C_{\varepsilon,\alpha}\dot{T} + \mathrm{div}\left(\underbrace{-\boldsymbol{k}\mathbf{grad}T}_{\mathbf{q}}\right) = \underbrace{\left(\sigma - \rho\psi_{,\varepsilon}\right) : \dot{\varepsilon} - \rho\psi_{,\alpha_k}\dot{\alpha}_k}_{\mathcal{D}_1} + \underbrace{\rho T\psi_{,T,\varepsilon} : \dot{\boldsymbol{\varepsilon}} + \rho T\psi_{,T,\alpha_k}\dot{\alpha}_k}_{\mathcal{W}_c} \tag{2}$$

where $\boldsymbol{k}$ denotes the heat conduction tensor and r_e the heat supply term characterizing the volume heat exchange with the surroundings.

The terms on the left hand side represent a partial differential operator applied to the temperature. The thermal inertia $\rho C_{\varepsilon,\alpha}\dot{T}$ reflects the stored or released heat rate. The term $-\mathrm{div}(\boldsymbol{k}\mathbf{grad}T)$ stands for the volume heat loss by conduction. The terms on the right hand side pool the different heat sources. In turn, we find the intrinsic mechanical dissipation $\mathcal{D}_1$, which reflects the irreversible transformation into heat of the deformation energy, the thermomechanical coupling sources $\dot{\mathcal{W}_c}$, which are the calorific signatures of the possible interactions between the temperature and the other state mechanical or microstructural variables.

2.2. Simplified heat source estimate models

Under certain experimental circumstances, some reasonable hypotheses to easily simplify Eq. (2) can be considered. The thermo-physical characteristics (ρ,$\boldsymbol{k}$,$C_{\varepsilon,\alpha}$) are considered as material constants independent of the thermodynamic state ($\boldsymbol{k}$ is also supposed isotropic, i.e. $\boldsymbol{k} = k\boldsymbol{\delta}$, where $\boldsymbol{\delta}$ is the identity tensor and k the isotropic conduction coefficient). The heat exchange r_e, here by radiation, is assumed to be time independent. As long as the displacement velocity amplitudes and temperature gradients remain low, the convective terms in the total time derivative of the temperature may also be neglected. Also, we assume that $\rho T\psi_{,T,\alpha_k}\dot{\alpha}_k \approx 0$ so that only the thermoelastic coupling effects are considered. The temperature averaged over the specimen thickness is approximately the same at the outer surfaces (*Berthel* et al. *(2008)* [14]).

Under the above hypotheses, it is possible to reduce Eq. (2) to the following two-dimensional diffusion model ([14]):

$$\rho C_{\varepsilon,\alpha}\left(\frac{\partial\overline{\theta}}{\partial t} + \frac{\overline{\theta}}{\tau_{th}^{2d}} - \frac{k}{\rho C_{\varepsilon,\alpha}}\left(\frac{\partial^2\overline{\theta}}{\partial x^2} + \frac{\partial^2\overline{\theta}}{\partial y^2}\right)\right) = \overline{\mathcal{D}}_1 + \overline{\dot{\mathcal{W}}}_{ther} \tag{3}$$

where $\overline{\theta} = \overline{T} - \overline{T}_o$ is the temperature averaged over the sample thickness ($\overline{T}_o$ denotes the initial temperature), τ_{th}^{2d} is a time constant characterizing heat losses perpendicular to the specimen surface.

By contrast with the two-dimensional approach and/or one-dimensional approach, similar to this introduced in *Chrysochoos and Louche (2000)* [15], the zero-dimensional approach is less sensitive to noise measurement and less time consuming in terms of computation time. This approach is well adapted to homogeneous tests when rapid experimental estimation of heat sources is required. This global approach is based essentially on the hypothesis that for uniaxial tests the heat source distributions are uniform throughout the test duration, within the specimen gauge area (linearisation of heat losses). Where θ denotes the spatial average of the function $\overline{\theta}$ over the gauge part (x and y coordinates), Eq. (3) can be simplified to:

$$\rho C_{\varepsilon,\alpha}\left(\dot{\theta} + \frac{\theta}{\tau_{th}^{0d}}\right) = \mathcal{D}_1 + \dot{\mathcal{W}}_{ther} \tag{4}$$

2.3. Deformation energy rate estimate

Under the small deformation hypothesis, the mechanical energy rate per unit volume $\dot{\mathcal{W}}_{def}$ developed during material deformation can be defined as follows:

$$\dot{\mathcal{W}}_{def} = \boldsymbol{\sigma} : \dot{\boldsymbol{\varepsilon}} \tag{5}$$

This energy rate is generally split into elastic $\dot{\mathcal{W}}_e$ and anelastic $\dot{\mathcal{W}}_{an}$ parts. The former part is the recoverable elastic energy rate per unit volume, and is calculated using the stress and elastic strain rate tensors. The latter part, i.e. the total anelastic energy rate per unit volume, is made of intrinsic dissipation $\mathcal{D}_1$ and stored energy rates per unit volume $\dot{\mathcal{W}}_s$. In this context, the deformation energy rate reads (*Chrysochoos (1985)* [7]):

$$\dot{\mathcal{W}}_{def} = \dot{\mathcal{W}}_e + \mathcal{D}_1 + \dot{\mathcal{W}}_s \tag{6}$$

Eq. (6) highlights the contribution of each component of the deformation energy rate. A correct estimate of $\dot{\mathcal{W}}_{def}$, $\mathcal{D}_1$, $\dot{\mathcal{W}}_e$ leads to indirect determination of $\dot{\mathcal{W}}_s$. Since the mechanical and heat energies are measured by two different techniques, systematic errors in one of the quantities do not cancel systematic errors in the measuring of the stored energy. In the case of uniaxial cyclic fatigue tests, the mechanical energy is commonly assessed by computing the area of the hysteresis loop. In the following, only the assessment over each complete cycle of the above volume energy rates will be considered. Thus, the elastic component per cycle remains close to zero and it can be considered that the mechanical and anelastic energy rates per unit volume per cycle are approximately the same $(\dot{\mathcal{W}}_{def})^{(n)} \approx (\dot{\mathcal{W}}_{an})^{(n)}$ (n represents the considered cycle). The key issue here is not only computing the stored energy rate per unit volume per cycle but also evaluating its contribution in the global energy balance. For this purpose, we define the variable stored energy rate ratio which is expressed by $\beta_s^{(n)} = (\dot{\mathcal{W}}_s)^{(n)}/(\dot{\mathcal{W}}_{def})^{(n)}$. The time courses of this ratio will be shown and analyzed in Subsec. 4.1.3. Note

that $\beta_s^{(n)}$ can be related to $\beta_{diff}^{(n)}$, introduced by Rittel in [10], to describe the dissipated part of the deformation energy rate: $\beta_{diff}^{(n)} = 1 - \beta_s^{(n)}$.

3. Experimental procedure

3.1. Experimental setup

The experimental setup used for conducting the thermomechanical tests is shown in Fig. 1. Samples were loaded using a MTS 810 hydraulic testing machine equipped with a load cell of ±25 kN. Temperature variations on one side and displacements on the other side of the sample were measured and captured simultaneously using a high resolution infrared focal plane array camera and a high resolution visible CCD camera, respectively.

Surface temperature fields corresponding to the rectangular gauge section were mapped using a Titanium IR camera (FLIR systems) with a frame rate ranging from 10 Hz to 100 Hz. The storage capacity of the camera was high enough to record successive images throughout the fatigue test. Several appropriate experimental precautions were taken. The camera was turned on for 4 h before starting the experiments in order to reach thermal equilibrium. The tested specimens were coated with black paint to improve the surface emissivity. The camera was calibrated using a black body (pixel calibration protocol, *Honorat* et al. *(2005)* [16]). It was positioned near the front of the sample and its lens axis was kept fixed and perpendicular to the gauge section during loading in order to collect reliable thermal data according to Lambert's law. A dummy specimen was placed close to the tested one to monitor possible temperature changes in the testing area. Some parts of the loading machine were wrapped with wrapping paper in order to avoid infrared parasitic reflections onto the specimen.

The visible images were recorded using a charged-coupled-device (CCD) camera (Phantom V12) with the same frame rates as that of the IRFPA camera. The surface in front of the CCD camera was sprayed with black paint (black background) and then speckled with white paint. The speckling was chosen such that the visible images remained contrasted. The purpose here was to build a virtual grid with local random optical signatures, with each optical signature characterizing a material surface element. The fields of superficial displacement associated with these optical signatures were determined using an in-house developed digital image correlation software package (the initial grid corresponds to the first image). Thus, both strains and strain rates were derived using spatial and temporal derivatives applied to the node displacements. As displacement assessments are inherently noisy, their derivatives were improved using a specific filtering and/or smoothing procedure based on the least squares method. The final signal retained the salient features of the original displacement record without the noisy component (*Wattrisse* et al. *(2001a)* [17]).

Note that IR and CCD cameras usually give acquisition errors at the beginning of recording. Even though both cameras start at the same time, the acquisition times are not necessarily the same. A shift in time acquisition for both cameras is usually observed and temporal readjustments are often required. A specific home-made electronic device (*Synchrocam*) was then designed to synchronize the visible and infrared acquisitions. To combine the thermal and kinetic data, the correspondence between the spatial coordinates of the thermal image (x_{IR},y_{IR}) and those of the visible image (x_{CCD},y_{CCD}) was established using rigid body motion (*Chrysochoos* et al. *(2009)* [18]).

3.2. Specimens and loading

Specimens of the PA6.6 dry matrix were tested at room temperature. All samples were provided by *Solvay*

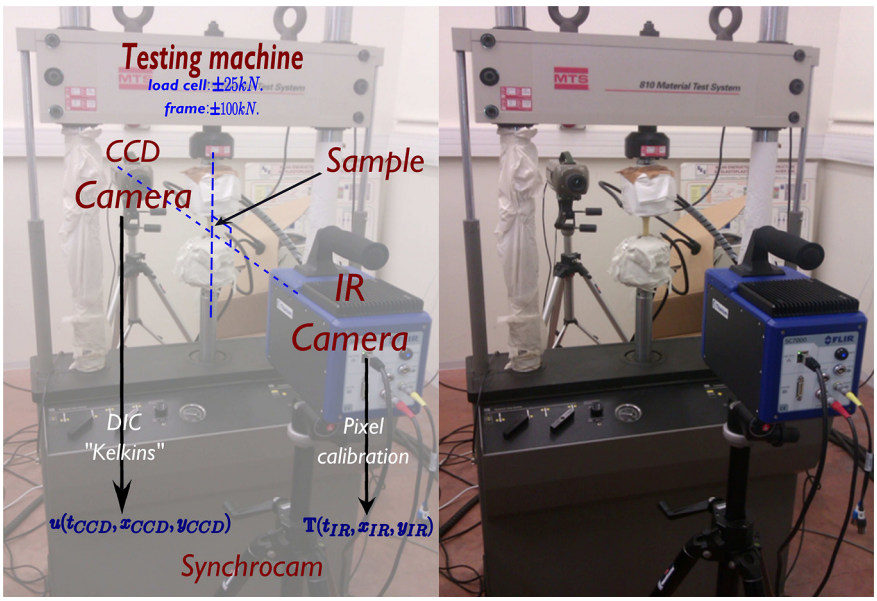

Fig. 1. Experimental setup showing both cameras used for recording the displacement and temperature surface fields.

Table 1
Thermophysical properties associated with the studied polyamide 6.6.

Material density (Kg m^{-1})	Heat capacity (J Kg^{-1} K^{-1})	Expansion coefficient (10^{-6} K^{-1})	Thermal conductivity (W K^{-1} m^{-1})	Thermal diffusivity (mm^2 s^{-1})
1120 ± 30	1638 ± 28	98 ± 13	0.343 ± 0.002	0.210 ± 0.004

Engineering Plastics and machined at *LMGC*. Some selected properties[2] from the material data sheet are given in Table 1. The sample geometry is outlined in Fig. 2.

Cyclic tensile-tensile loads were carried out under a stress ratio of 0.1. The loading frequency ranged from 1 to 10 Hz, while the number of cycles was 10^4. The cycle number was high enough to raise the kinematic and thermal properties of the investigated materials. The mechanical loading is illustrated in Fig. 3.

At the beginning of the test, the load signal was set at zero for 10 s to calculate the stabilized thermal image. Its displacement rate was then controlled with a constant cross-head velocity of 1 mms^{-1}, stress maintained at σ_{min} for 3 s with tensile-tensile loading between σ_{min} and σ_{max}.

4. Experimental results

The experimental study involved observation and analysis of the thermomechanical and energy properties of the PA6.6 dry matrix involved during cyclic fatigue tests. The investigations were essentially divided into two parts. The first part examined, at two different loading frequencies, the contribution of the stored and dissipated energies in the global energy balance. The second part focused on the localization of fatigue mechanisms using 2d full-field measurements through the heterogeneous distribution of the energy response.

4.1. Energy balance: 0d approach

4.1.1. Quasi-uniform patterns of the calorific data

The starting point of this experimental work was evaluating local heat sources that take place during cyclic loading of PA6.6 dry specimens. Local assessment of these sources is crucial when establishing local energy balances. The purpose here was to collect more information on the energy behavior of PA6.6. These energy signatures will facilitate the future modelling of this semi-crystalline thermoplastic matrix.

Fig. 4 shows patterns of the temperature variation $\overline{\theta}$, the mean dissipation per cycle $\overline{\mathcal{D}_1}$ and the thermoelastic source amplitudes $\overline{\Delta s_{ther}}$, ery first fatigue stages in a PA6.6 dry specimen subjected to a tensile-tensile test. The size of the selected images is roughly equivalent to a box of 23.20 mm in length by 11.42 mm in width, covering approximately 42% of the global specimen surface. The spatial resolution is 0.357 mm/pixel. All images were obtained after spatio-temporal smoothing of the thermal data recorded by the

[2] The thermo-physical data were determined using different experimental equipment. The expansion coefficient was measured using a *Netzsch Dil 402C dilatometer*, while the other thermal properties were calculated using a *Hot Disk thermal analyser*.

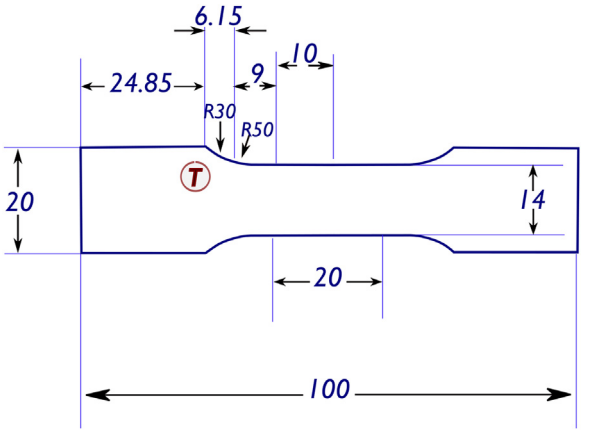

Fig. 2. Shape of the specimens used for the experiments (all dimensions are in millimetres). The thickness ranged from 3.15 mm to 3.28 mm.

IR camera. The computation time required for this smoothing process and heat source assessment was very high, naturally depending on the computational resources. For a 3 GHz processor, the time necessary to compute a heat source map is about 1 min with a standard test containing up to $2 \cdot 10^6$ images. The mean value and standard deviation associated with these thermal distributions are given in Table 2.

According to Fig. 4, we observed quasi-uniform patterns in the selected thermal and calorimetric data. The standard deviation associated with these calorimetric data fields only reached 0.045 °C for temperature variations (0.0006 °C s^{-1} and 1.25 °C s^{-1} for dissipation and thermoelastic sources, respectively) at the first step and only 0.061 °C (0.0037 °C s^{-1} and 1.27 °C s^{-1} respectively) at the second one. This means that the values were all clustered close to the spatial average. Despite the fact that weak thermal gradients were noted at the boundary of the images with their typical associated colorbar, it can be considered that there was quite good spatial homogeneity

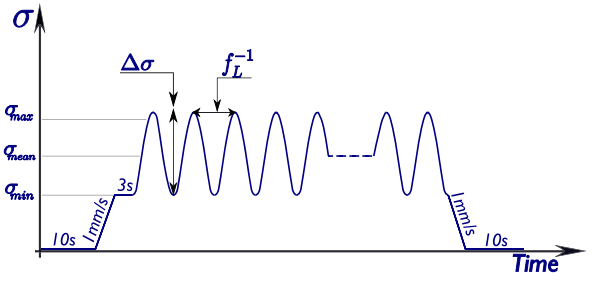

Fig. 3. Diagram of the mechanical loading used in the experiments.

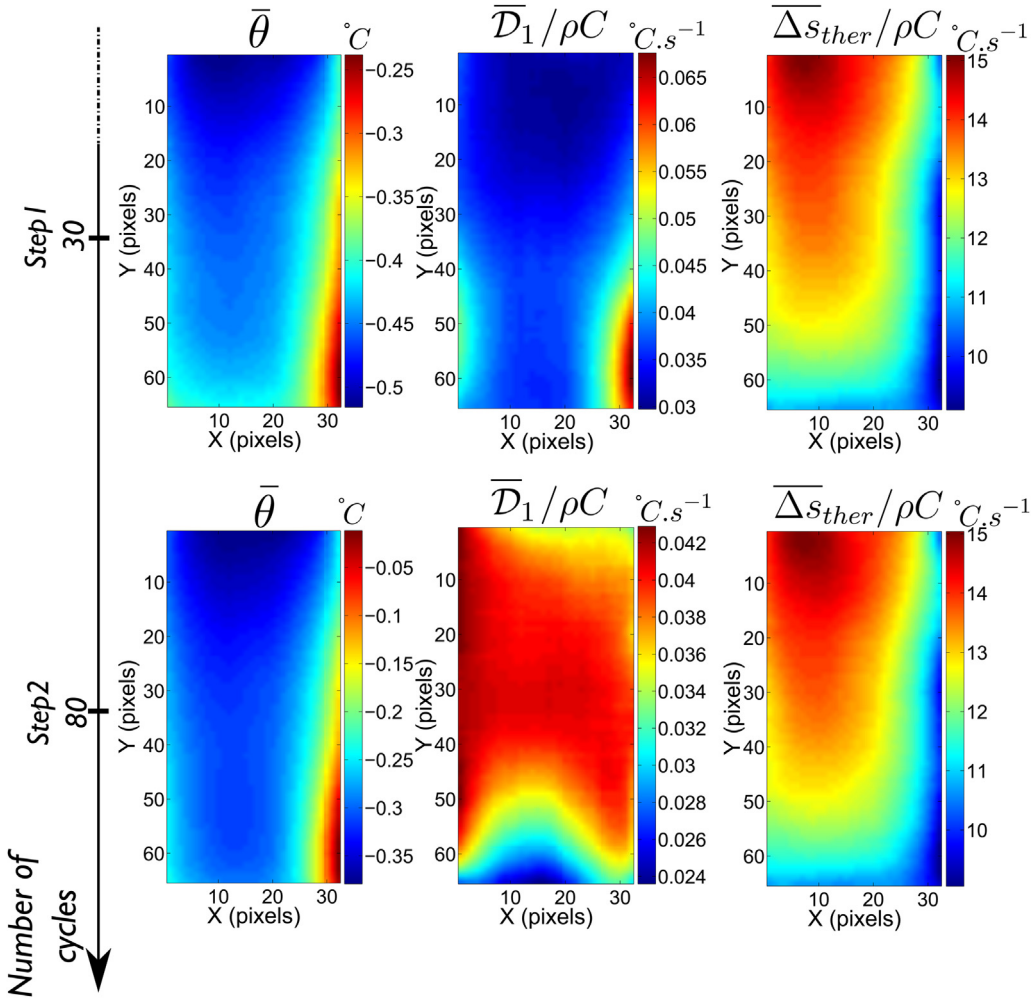

Fig. 4. Maps associated with the temperature variations, the mean intrinsic dissipation per cycle and the thermoelastic source amplitudes, taken at the first fatigue stages (steps 1 and 2) of a PA6.6 dry specimen. The spatial resolution is 0.357 mm/pixel. N_c denotes the number of cycles.

in all the patterns. These least spatial heterogeneities that we have at the image borders are essentially due to artefacts and/or spatial smoothing. As a first approximation, it can be considered that the heterogeneities are negligible and that all the spatial distributions are spread in an homogeneous manner throughout the loading, or at least during a certain part of the loading. This hypothesis will considerably reduce the computation time and allow us to study overall energy balance trends with the global approach, as noted in Eq. (4).

Table 2
The spatial average and standard deviation associated with the selected thermal cards mentioned in Fig. 4.

	Cycling stages	Spatial average	Standard deviation
$\overline{\theta}$ (°C)	Step 1	−0.44	0.047
	Step 2	−0.29	0.0610
$\overline{\mathcal{D}}_1/(\rho C)$ (°C s^{-1})	Step 1	0.0368	0.006
	Step 2	0.038	0.004
$\overline{\Delta s}_{\mathrm{ther}}/(\rho C)$ (°C s^{-1})	Step 1	12.63	1.25
	Step 2	12.63	1.27

4.1.2. Mechanical and thermal responses

4.1.2.1. Cyclic stress-strain curves. The spatio-temporal displacement distributions were assessed using in-house developed digital image correlation software "*Kelkins*" (see e.g. *Bornert* et al. *(2009)* [19]). The applied load was measured by a load cell mounted on the hydraulic testing machine. The different components (tensile, shear and contraction) of the local stress tensor were derived from the equilibrium equations based on several assumptions[3]:

$$\sigma_{yy}(y,t) = \frac{f(t)}{S_o}\exp\left(\varepsilon_{yy}(y,t)\right) \tag{7}$$

$$\sigma_{xy}(x,y,t) = -\sigma_{yy}(y,t)\frac{\partial \varepsilon_{yy}(y,t)}{\partial y}x \tag{8}$$

[3] The assumptions detailed in *Wattrisse* et al. *(2001b)* [20] are: *i)* plane stress pattern, *ii)* material incompressibility, *iii)* no overall shear loading and *iv)* lateral surfaces of the specimen free of stress.

$$\sigma_{xx}(x,y,t) = \frac{\partial}{\partial y}\left(\frac{\sigma_{yy}(y,t)}{2}\frac{\partial \varepsilon_{yy}(y,t)}{\partial y}\right)\left(\frac{l^2(y,t)}{4} - x^2\right) \quad (9)$$

where f represents the load, S_o the initial cross-section, ε_{yy} the longitudinal component of Hencky strain and l the sample width.

Using displacement data obtained by DIC techniques, the in-plane strain fields of the Hencky strain tensor can be assessed. Fig. 5(a) shows the spatial distribution of the longitudinal strain component ε_{yy} for three fatigue stages. The strain fields remained approximately uniform with the stress fields derived from Eqs. (7)–(9).The contribution of the transversal and shear stress and strain-rate components to the computation of the deformation energy rate remained negligible, as shown in Fig. 5(b). As the image processing required high CPU time, we decided to only consider the mean (spatially averaged) tensile stress and longitudinal strain rate to compute the deformation energy rate.

The influence of the loading frequency on the mechanical response is hereafter discussed. The spatial average of longitudinal stress-strain curves associated with the investigated specimens are shown in Fig. 6. Two different loading frequencies were chosen, i.e. a low frequency of 1 Hz and a high frequency of 10 Hz. Only stresses normalized by the yield stress of the Pa6.6 matrix are indicated and the theoretical values will not be mentioned. Note in this figure that the loops associated with the low loading frequency are much thinner compared to those in high loading frequency. As can also be seen, both hysteresis curves never reach a steady-state after a sufficiently high number of cycles. Consequently, there was no clear cyclic adaptation and no cyclic state of stabilization after the first few cycles. At the same stress amplitude, a significant loop shifting, i.e. ratcheting phenomenon, characterized by an accumulation of cyclic strain was observed. This broadening in loops was less pronounced in Fig. 6 (plot (b)) whereas it was significant in Fig. 6 (plot (a)).

The hysteresis loops usually offer useful information on the material state. The energy content of these mechanical loops is of particular interest when characterizing the mechanical and energy behavior of loaded specimens. Indeed, it is still commonly acknowledged in the literature that the deformation energy loss is essentially due to material dissipation. Hence, the area of the surface enclosed within the hysteresis loop always equals the amount of energy dissipated in the material over a complete loading cycle. However, from a thermodynamic standpoint, it has been shown that, although intrinsic dissipation naturally contributes to the existence of a hysteresis loop, other phenomena may also modify the size of its area. Recently, *Chrysochoos (2012)* [21] illustrated, through several experiments on a wide range of materials, that the hysteresis area may not only be induced by intrinsic dissipation but also by internal energy variations due to microstructural transformations and/or strong thermomechanical coupling effects. This energy analysis will be summarized and strengthened by the experimental results in Subsec. 4.1.3.

4.1.2.2. Thermal response. For the sake of simplicity, the mean temperature variations averaged over the sample gauge part are first considered. Typical plots associated

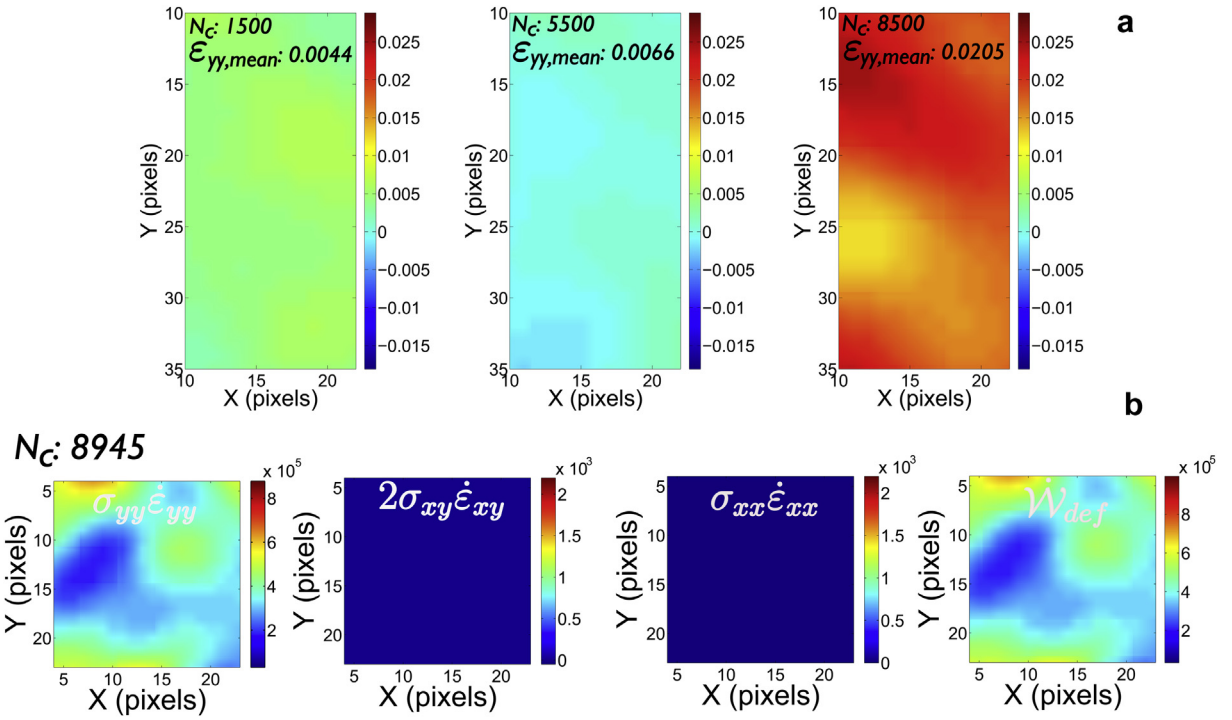

Fig. 5. Maps of (a) longitudinal strain component taken at three fatigue stages, (b) deformation energy rates (longitudinal, transversal, shear contributions and overall estimate). The spatial resolution is 0.251 mm/pixel. N_c denotes the number of cycles.

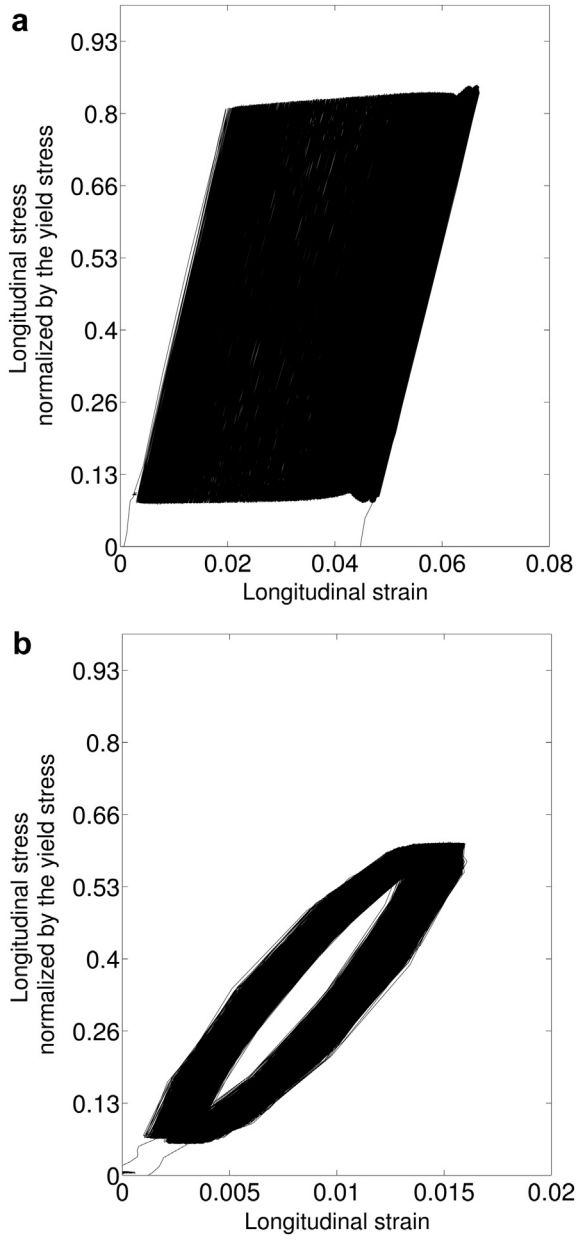

Fig. 6. Spatial average of stress-strain hysteresis loops for PA6.6 dry matrix specimens subjected to (a) a low loading frequency of 1 Hz and (b) a high loading frequency of 10 Hz. The stress ratio is 0.1 and the number of cycles is 10^4.

with these thermal variations as a function of time (image number) and at both studied loading rates are shown in Fig. 7.

Conventionally, temperature variations involve low frequency drifts with an oscillation in opposite phase with the monochromatic loading signal. We associated two independent heat sources with both of these thermosignal characteristics. The oscillation is induced by the thermoelastic source coming from the material thermodilatability. The heating of the specimen is associated with the dissipated energy. It is often characterized by a progressive global increase in temperature variations. A decrease in mean temperature is associated with a decrease in the dissipation intensities, with the heat exchange coefficients between the specimen and the surroundings assumed to be constant throughout the test. From a calorimetric viewpoint, it was found that the intrinsic dissipation intensities remained very low compared with the ranges of the thermoelastic source amplitudes. These calorimetric analysis will be summarized in Subsec. 4.2.

One last point to be discussed is regarding the dispersion of thermal data. For identical test conditions (e.g. same material, loading rate, hygrothermal conditions and stress level), two loaded samples may not necessarily exhibit the same thermal response (Fig. 7 (plots (a) and (b))). This means that the global balances of energy rates associated with these samples will not necessarily be quantitatively similar, and only the main trend will be considered. This spread may be due to the initial microstructural state of both specimens extracted from the same PA6.6 plate but at different places. The results shown in Fig. 7 (plots (a) and (b)) were specially chosen to underline these quantitative variations in behavior that must be considered in the industrial design.

4.1.3. Loading frequency effect

In the following, the global energy response of the studied material is analyzed. The mean deformation energy rate, averaged over a complete cycle $\tilde{\dot{\mathcal{W}}}_{\text{def}}$, the mean stored energy rate $\tilde{\dot{\mathcal{W}}}_{\text{s}}$ and the mean dissipation $\tilde{\mathcal{D}}_1$ were systematically plotted. The mean elastic energy rate averaged over a loading cycle was negligible, and thus not plotted. The energy results corresponding to both studied loading frequencies are shown in Figs. 8 and 9. All the energy rates were assessed using the thermomechanical equations and post-processing of the experimental data. The mean dissipation energy rate over a cycle $\tilde{\mathcal{D}}_1$ was calculated via the zero-dimensional approach of the local heat diffusion equation (Eq. (4)). The mechanical energy rate per cycle was estimated using the expression below:

$$\tilde{\dot{\mathcal{W}}}_{\text{def}} = f_L \mathcal{R} \frac{\int F_{\text{mts}} dl_{\text{mts}}}{V_{\text{g}}} \tag{10}$$

where F_{mts}, dl_{mts} and V_g are respectively the applied force, the global elongation and the volume of the gauge area. $\mathcal{R}$ represents a geometrical ratio characteristic of the loaded specimen. This ratio connects the global mechanical response to the local one based on the hypothesis that the deformation process is homogeneous over each cross-section. It was calculated using the following equation:

$$\mathcal{R} = \int_{-\frac{L_o}{2}}^{\frac{L_o}{2}} l^{-1}(x)dy \Big/ \int_{-\frac{L}{2}}^{\frac{L}{2}} l^{-1}(x)dy \tag{11}$$

L_o denotes the length of the gauge section while L represents the global length of the sample.

From all the plots, it can be observed that the overall shape of the energy rate balance closely depends on the loading frequency. For a dry matrix at a high loading rate ($f_L = 10$ Hz), the results indicate a substantial part of the

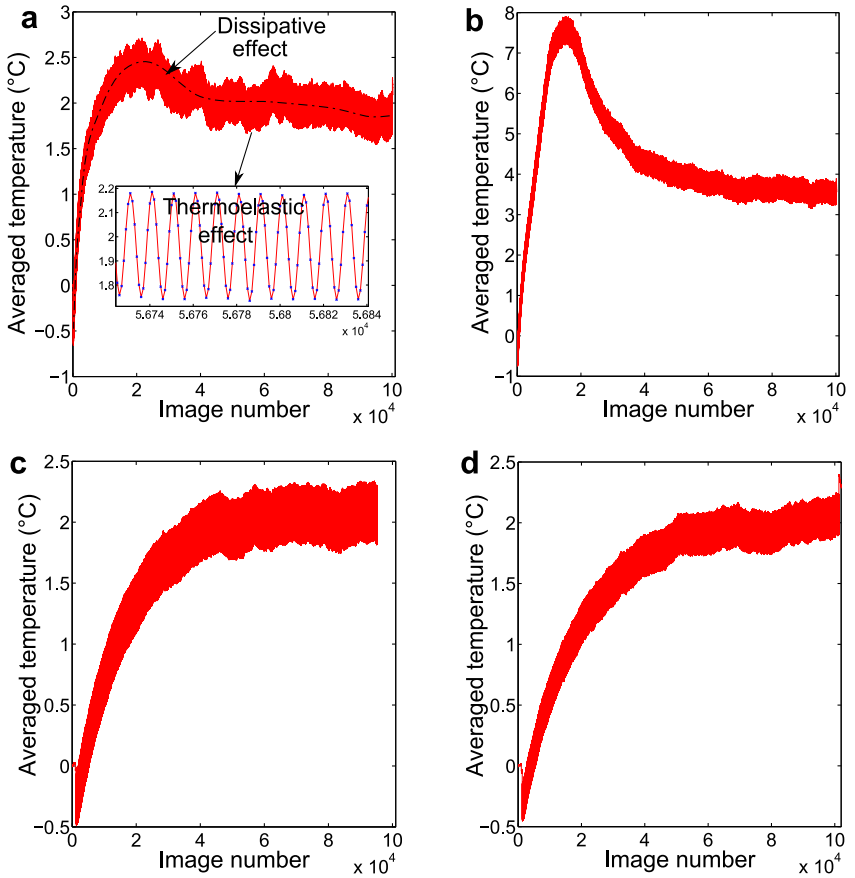

Fig. 7. Spatial average of the thermal response for PA6.6 matrix specimens. ((a) The first test with $f_L = 1$ Hz, (b) the second test with $f_L = 1$ Hz, (c) the first test with $f_L = 10$ Hz and (d) the second test with $f_L = 10$ Hz.)

mean stored energy rate per cycle has a ratio near 83% (Fig. 8, plot (b)). This part dominates the mean intrinsic dissipation per cycle whose ratio seems to be stabilized around 17%. However, in the case of low loading frequencies ($f_L = 1$ Hz), the trend of these variable ratios changes completely (Fig. 9). The mean intrinsic dissipation per cycle is now predominant compared with the stored energy rate. It starts increasing at the beginning of loading and then stabilizes after the first few cycles, with a ratio of 73% (Fig. 9, plot (b)) and 65% (Fig. 9, plot (d)). Our studies so far have shown that the mean mechanical energy over a complete cycle exceeded the heat generated. The strained sample could generally not dissipate more heat than it received. However, in some cases the heat is observed to be generated at a higher rate than the mechanical energy, indicating a release of stored energy (see e.g. *Dillon (1966)* [22], Rittel (1999) for polymers and *Oliferuk* et al. *(2001)* [23] for metals). Fig. 10 illustrates a case of a PA6.6 specimen that released more heat than the mechanical energy at the last stages of its fatigue life. Thermal and kinetic images have were recorded until the final rupture of the specimen (2531 cycles), allowing us to study the trend of the global energy balance close to the macroscopic crack. In this figure, the ratio of the stored energy rate over a complete cycle falls continuously with the test time. The amount of the stored energy rate is high at the beginning of loading and then decreases as the test proceeds, until reaching negative values at the end of loading. This highlights a rapid increase in intrinsic dissipation, thus indicating a higher amount of mechanical energy converted into heat. Even at low frequencies, the stored proportion remains high and can then represent a slow but regular material degradation.

Another point to be discussed is the hypothesis of quasi-uniform patterns. This hypothesis gives only a global view of energy balance patterns. Due to the manner by which these balances tend to vary, especially in Fig. 10, it is essential to look at what can locally happen, notably when a crack appears in the specimen. Instead of drawing up the global energy rate balance, it is important to focus on the local one. This local analysis is addressed in the next subsection.

4.2. Calorimetric analysis of the fatigue kinetics

The current investigation is intended to establish a correlation between the increase in heat data and the variations in the fatigue kinetics. It focuses essentially on

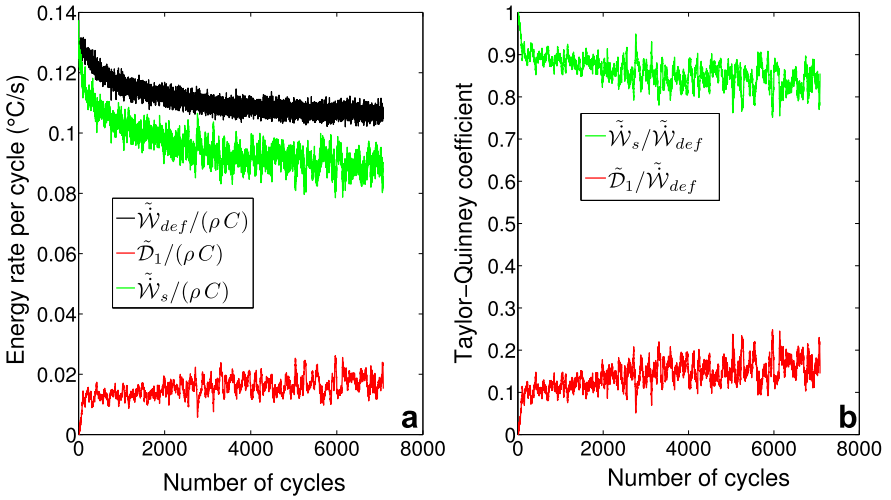

Fig. 8. (a) The energy rate balance for the PA6.6 dry matrix and its (b) corresponding Taylor-Quinney evolution. The loading frequency is equal to10 Hz, the load ratio is $R_\sigma = 0.1$. $\mathcal{R} = 0.42$ and $V_g = 6.2 \cdot 10^{-7}$ m^3.

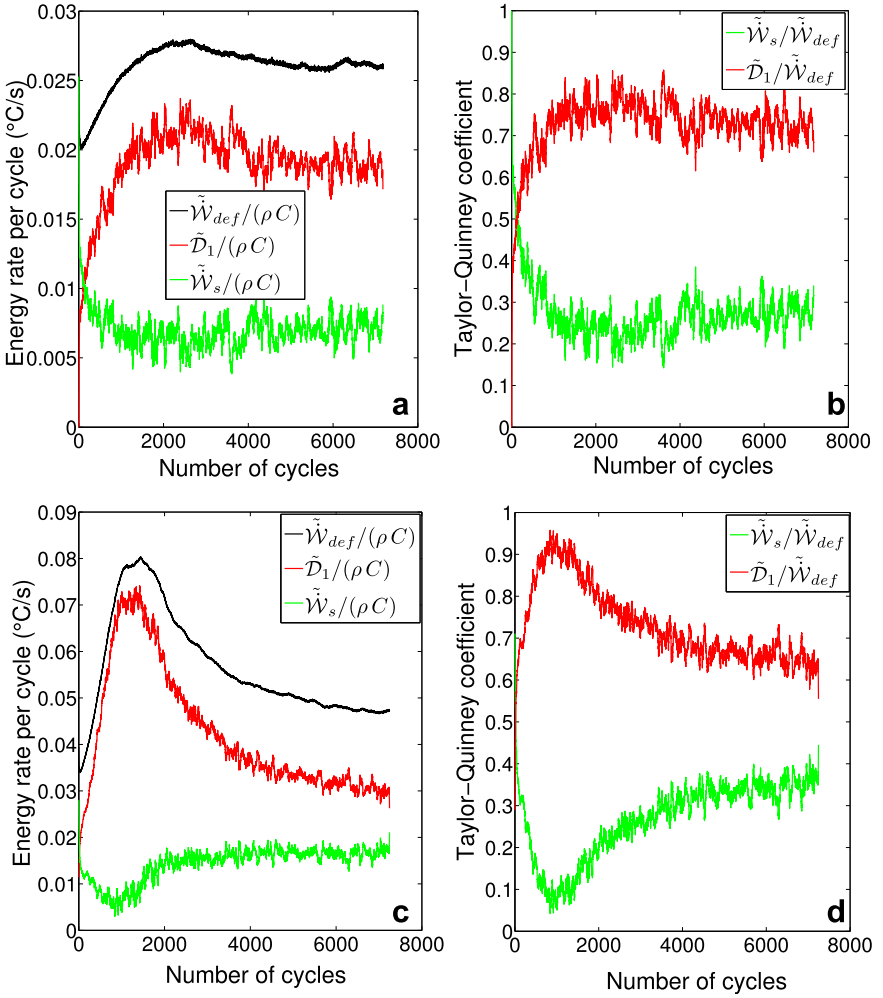

Fig. 9. The energy rate balance for the PA6.6 dry matrix ((a) the first test, (b) Taylor-Quinney of the first test, (c) the second test (d) Taylor-Quinney of the second test). The loading frequency is equal to 1 Hz, while the load ratio is $R_\sigma = 0.1 \mathcal{R} = 0.437$ and $V_g = 7.53 \cdot 10^{-7}$ m^3.

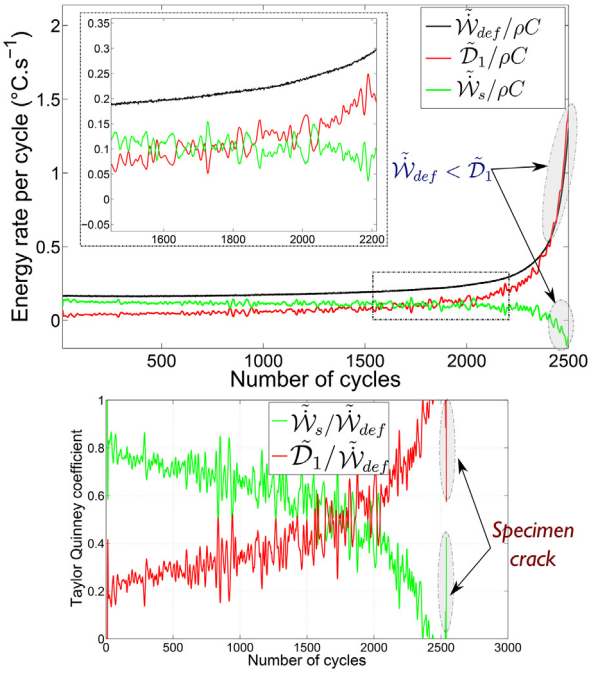

Fig. 10. The energy rate balance for a PA6.6 dry matrix from the beginning of cyclic loading until the last few cycles before the macroscopic crack. The loading frequency is equal to 10 Hz, and the load ratio is $R_\sigma = 0.1$. $\mathcal{R} = 0.48$ and $V_g = 8.49 \cdot 10^{-7}$ m^3.

detection of the hottest area that occurs in the dissipation pattern. The challenge is thus to combine thermoelastic source amplitudes and intrinsic dissipation fields in order to detect local degradation in the specimen during fatigue testing, and at the same time to get information on the dissipative and thermoelastic mechanisms connected to the constitutive equations.

Thermoelastic coupling causes a temporal variation in the temperature field during mechanical loading, i.e. a temperature drop during loading and a temperature rise during unloading. This reversible change in temperature is supposed to be proportional to the change in the first stress invariant, as shown by *William Thomson (Lord Kelvin) in 1851* [24], and more recently discussed in *Boulanger and al. (2004)* [25]. In the following, the large stress concentration areas are quantified via thermoelastic fields while the sensitive zones, where the examined specimen dissipated more, are located by intrinsic dissipation fields.

The selected images in Fig. 11 represent different thermal maps of a PA6.6 dry specimen subjected to a cyclic fatigue test. Each image is referred by the number of cycles, over which the average image is performed. These images highlight the last few stages in the fatigue life of the specimen. The spatial heterogeneities were clearly visible throughout all the selected fatigue steps. The images at 2488 show a relatively healthy specimen with weak heat and stress localizations. From 2488 to 2527 cycles, the temperature variations, the mean intrinsic dissipation per cycle and the thermoelasticity amplitude increase sharply in some specific locations. Indeed, it is clear that initially the heterogeneities started to propagate horizontally, as indicated by the images. Then, after a few cycles, these local spatial heterogeneities became curved. This could probably be attributed to shear stresses resulting from the unidirectional tensile external load and/or the pre-existing local defects that can act as temperature release points. The rapid increase in heat intensity, i.e. within a few cycles, could indicate an imminent crack in the loaded specimen. Even the magnitudes of the thermoelastic source amplitudes were higher (250 °C s^{-1} at the hottest zone) compared those of the mean intrinsic dissipation (8 °C s^{-1} at the hottest zone), while the mean temperature of the specimen is not necessary affected by this reversible thermocoupling source. By contrast, the always positive dissipation caused a continuous mean temperature rise (Fig. 7) for the cyclic loading and could cause the final rupture of the loaded specimen.

The above investigation into the progress of spatial heterogeneities demonstrates that calorimetric analysis is a suitable powerful experimental tool that can be used to investigate localized hot spots. It has the potential to provide local information on dissipation and stress fields in an investigated specimen. This thermographic methodology will still be used in subsequent studies which are already under way, especially for investigating the fiber orientation effect in fiber-reinforced polymeric materials (Fig. 12).

5. Concluding comments

Some aspects related to thermal and energy responses associated with PA6.6 dry specimens subjected to tensile-tensile tests were investigated in this work. The first aspect was the loading frequency dependence of energy balances. The investigations of energy stored during deformation indicated that the stored ratio was significantly smaller at low loading rates but remained high at high loading rates. In addition, it was shown that this ratio may take negative values at the last fatigue stages before the macroscopic crack, which could be attributed to the release of stored energy in form of heat.

Calorimetric analyses were also conducted at the end of the fatigue life to localize hotspots that occur in intrinsic dissipation and thermoelastic fields. This generated some insight into the contribution of these mechanisms in producing point defects. It has been shown that the spatial local heterogeneities started to propagate horizontally and then, after few cycles, became curved, indicating an imminent crack in the loaded specimen. Even without the complications associated with the experimental equipment, this investigation of fatigue kinetics confirmed that the calorimetric methodology could potentially provide local information especially on dissipation and stress distributions. Further experiments are required to obtain a better understanding of the effects of these mechanisms, especially in fiber-reinforced polymeric materials in which the fiber orientation effect has to be explored. Future investigations will also deal with the role of humidity on the PA 6.6 cyclic behavior.

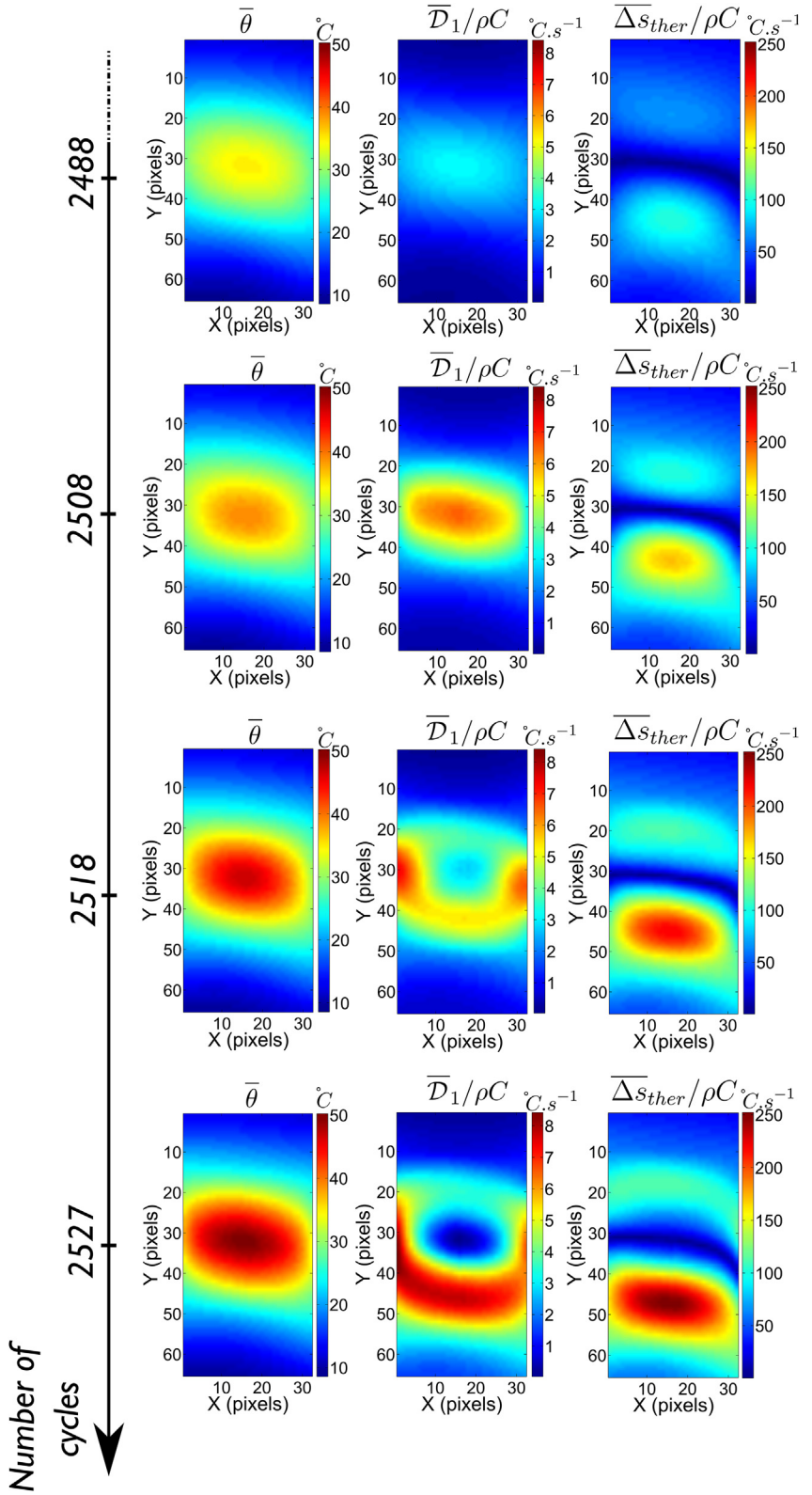

Fig. 11. Fields of the temperature variations, the mean intrinsic dissipation per cycle and the thermoelasticity amplitude, taken at the last fatigue stages of a PA6.6 dry specimen. The spatial resolution is 0.357 mm/pixel.

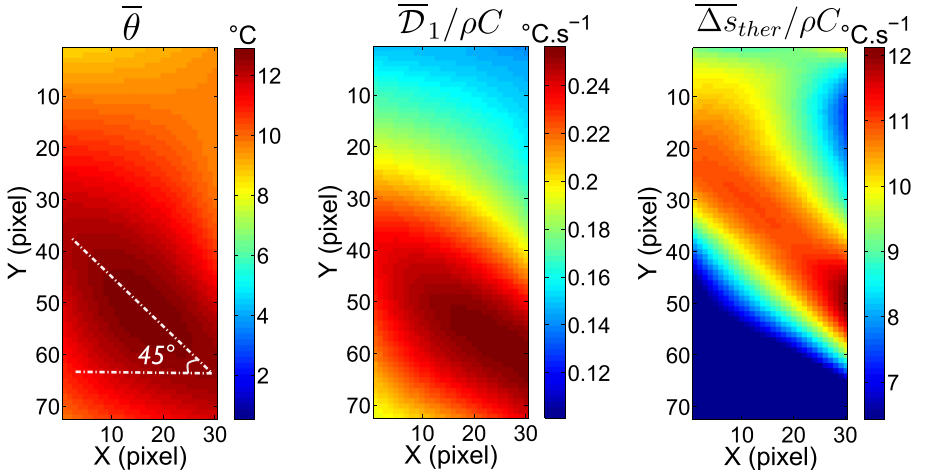

Fig. 12. Fields of the temperature variations, the mean intrinsic dissipation per cycle and the thermoelastic source amplitudes of a PA6.6 specimen reinforced with short glass fibers oriented at 45. The spatial resolution is 0.357 mm/pixel.

Acknowledgements

The authors gratefully acknowledge Solvay Engineering Plastics for supporting this work and for providing material data and specimens. This work benefited from the financial support of the French Minister for Research (ANRT) and was performed in the framework of the European *DURAFIP* project.

References

[1] D. Rittel, An investigation of the heat generated during cyclic loading of two glassy polymers. Part I: experimental, Mech. Mater. 32 (2000) 131–147.

[2] D. Rittel, Y. Rabin, An investigation of the heat generated during cyclic loading of two glassy polymers. Part II: thermal analysis, Mech. Mater. 32 (2000) 149–159.

[3] W.S. Farren, G.I. Taylor, The heat developed during plastic extension of metals, Proc. R. Soc. A Math. Phys. Eng. Sci. 107 (1925) 422–451.

[4] G.I. Taylor, H. Quinney, The latent energy remaining in a metal after cold working, Proc. R. Soc. A Math. Phys. Eng. Sci. 143 (1934) 307–326.

[5] R.O. Williams, in: H. Herman (Ed.), Experimental Methods of Materials Research, vol. 1, Interscience, 1967.

[6] J.S.L.L. Leach, in: R.A. Rapp (Ed.), Physicochemical Measurements in Metals Research, vol. 4, Interscience, 1970.

[7] A. Chrysochoos, Energy balance for elastic plastic deformation at finite strain (in French), J. Méc. Théor. Appl. 5 (1985) 589–614.

[8] A. Chrysochoos, O. Maisonneuve, G. Martin, H. Caumon, J.C. Chezeaux, Plastic and dissipated work and stored energy, Nucl. Eng. Des. 114 (1989) 323–333.

[9] J. Mason, A. Rosakis, G. Ravichandran, On the strain and strain rate dependence of the fraction of plastic work converted to heat: an experimental study using high speed infrared detectors and the Kolsky bar, Mech. Mater. 17 (1994) 135–145.

[10] D. Rittel, On the conversion of plastic work to heat during high strain rate deformation of glassy polymers, Mech. Mater. 31 (1999) 131–139.

[11] P. Rosakis, A.J. Rosakis, G. Ravichandran, J. Hodowany, A thermodynamic internal variable model for the partition of plastic work into heat and stored energy in metals, J. Mech. Phys. Solids 48 (2000) 581–607.

[12] W. Oliferuk, M. Maj, B. Raniecki, Experimental analysis of energy storage rate components during tensile deformation of polycrystals, Mater. Sci. Eng. A Struct. Mater. Prop. Microstruct. Process. 374 (2004) 77–81.

[13] B. Halphen, Q.S. Nguyen, On the generalized standards materials (in French), J. Méc. 14 (I) (1975) 39–63.

[14] B. Berthel, A. Chrysochoos, B. Wattrisse, A. Galtier, Infrared image processing for the calorimetric analysis of fatigue phenomena, Exp. Mech. 48 (2008) 79–90.

[15] A. Chrysochoos, H. Louche, An infrared image processing to analyse the calorific effects accompanying strain localisation, Int. J. Eng. Sci. 38 (2000) 1759–1788.

[16] V. Honorat, S. Moreau, J.M. Muracciole, B. Wattrisse, A. Chrysochoos, Calorimetric analysis of polymer behaviour using a pixel calibration of an IRFPA camera, QIRT J. 2 (2005) 153–171.

[17] B. Wattrisse, A. Chrysochoos, J.-M. Muracciole, M. Némoz-Gaillard, Analysis of strain localization during tensile tests by digital image correlation, Exp. Mech. 41 (2001) 29–39.

[18] A. Chrysochoos, B. Wattrisse, J.-M. Muracciole, Y. El Kaïm, Fields of stored energy associated with localized necking of steel, J. Mech. Mater. Struct. 4 (2009) 245–262.

[19] M. Bornert, F. Brémand, P. Doumalin, J.-C. Dupré, M. Fazzini, M. Grédiac, F. Hild, S. Mistou, J. Molimard, J.-J. OrteuL, L. Robert, Y. Surrel, P. Vacher, B. Wattrisse, Assessment of digital image correlation measurement errors: methodology and results, Exp. Mech. 49 (2009) 353–370.

[20] B. Wattrisse, A. Chrysochoos, J.M. Muracciole, M. Némoz-Gaillard, Kinematic manifestations of localisation phenomena in steels by digital image correlation, Eur. J. Mech. A/Solids 20 (2001) 189–211.

[21] A. Chrysochoos, Thermomechanical analysis of the cyclic behavior of materials, Proc. IUTAM 4 (2012) 15–26.

[22] O.W.J. Dillon, The heat generated during the torsional oscillations of copper tubes, Int. J. Solids Struct. 2 (1966) 181–204.

[23] W. Oliferuk, A. Korbel, W. Bochniak, Energy balance and macroscopic strain localization during plastic deformation of polycrystalline metals, Mater. Sci. Eng. A Struct. Mater. Prop. Microstruct. Process. 319 (2001) 250–253.

[24] W. Thomson, On the dynamical theory of heat, Trans. R. Soc. 20 (1853) 261–283.

[25] T. Boulanger, A. Chrysochoos, C. Mabru, A. Galtier, Calorimetric analysis of dissipative and thermoelastic effects associated with the fatigue behavior of steels, Int. J. Fatigue 26 (2004) 221–229.